This is a repository copy of *A fully coupled fluid-structure interaction simulation of three-dimensional dynamic ductile fracture in a steel pipeline*.

A fully coupled fluid-structure interaction simulation of three-dimensional dynamic ductile fracture in a steel pipeline

Reza Talemi[*,1,2], Steven Cooreman[1], Haroun Mahgerefteh[3], Sergey Martynov[3], Solomon Brown[4]

[1]ArcelorMittal Global R&D Gent-OCAS N.V., Pres. J.F. Kennedylaan 3, 9060 Zelzate, Belgium.

[2] Present address: Department of Materials Engineering, KU Leuven, 3001 Leuven, Belgium

[3]Department of Chemical Engineering, University College London, London, WC1E7JE, UK

[4]Department of Chemical and Biological Engineering, The University of Sheffield, S1 3JD, UK

Corresponding Author[*]: Reza Talemi, reza.hojjatitalemi@kuleuven.be

Abstract

Long running fractures in high-pressure pipelines transporting hazardous fluid are catastrophic events resulting in pipeline damage and posing safety and environmental risks. Therefore, the ductile fracture propagation control is an essential element of the pipeline design. In this study, a coupled fluid-structure interaction modelling is used to simulate the dynamic ductile fractures in steel pipelines. The proposed model couples a fluid dynamics model describing the pipeline decompression and the fracture mechanics of the deforming pipeline exposed to internal and back-fill pressures. To simulate the state of the flow in a rupturing pipeline, a compressible one-dimensional computational fluid dynamics model is applied, where the fluid properties are evaluated using a rigorous thermodynamic model. The ductile failure of the steel pipeline is described as an extension of the modified Bai-Wierzbicki model implemented in a finite element code. The proposed methodology has successfully been applied to simulate a full-scale pipeline burst test performed by British Gas Company, which involved rupture of a buried X70 steel pipeline, initially filled with rich natural gas at 11.6 MPa and –5 °C.

Keywords: Ductile fracture; Fluid-structure interaction model; Steel pipeline; HLP; XMBW; CFD

Nomenclature

Acronyms

BGC	British Gas Company
BTC	Battelle Two Curve
BW	Bai-Wierzbicki
CDM	Continuum Damage Mechanics
CFD	Computational Fluid Dynamics
CVN	Charpy V-Notch
DWTT	Drop Weight Tear Test
FBR	Full-Bore Rupture
FEM	Finite Element Modelling
GTN	Gurson-Tvergaard-Needleman
HEM	Homogenous Equilibrium Mixture
HLP	High-Strength Line Pipe
MBW	Modified Bai-Wierzbicki
XMBW	Extended Modified Bai-Wierzbicki

Symbols

σ'_{ij}	deviatoric stress tensor
$\dot{\bar{\varepsilon}}_p$	equivalent plastic strain rate
$\bar{\varepsilon}_p$	equivalent plastic strain
$\bar{\sigma}(\bar{\varepsilon}_p)$	flow curve
$\bar{\theta}$	normalized load angle
Δt	small time increment
δ_{ij}	Kronecker delta
$\dot{a}$	crack propagation speed
$\dot{D}$	damage evolution rate
η	stress triaxiality
η_0	reference stress triaxiality (=1/3)

$\hat{\varepsilon}_i(\eta,\overline{\theta})$	plastic strain at crack initiation
$\hat{\varepsilon}_f(\eta,\overline{\theta})$	three-dimensional fracture locus
∂Z	short interval of pipe cross-sectional area
∂Z_f	effective area of smoothing distance
Φ	yield potential function
ρ	fluid density
ρ_l	density of liquid phase
ρ_v	density of vapor
σ_y^i	yield stress at onset of damage
$\sigma_1, \sigma_2, \sigma_3$	principal stresses
σ_{eq}	equivalent stress
σ_f	material flow stress
σ_{ij}	stress tensor
σ_m	mean stress
σ_{ult}	ultimate tensile stress
σ_y	yield stress
θ	Lode angle
ξ	normalized third stress tensor
A	pipe cross-section
A_0	initial pipe cross-section
A_f	effective area of expanded pipe
A_p	ligament area of pre-cracked DWTT
$c_{\dot{\overline{\varepsilon}}}^1, c_{\dot{\overline{\varepsilon}}}^2, c_{\dot{\overline{\varepsilon}}}^3$	strain rate correction material parameters
c_T^1, c_T^2, c_T^3	temperature correction material parameters
$c_\theta^t, c_\theta^s, c_\theta^c, c_\theta^{ax}, \lambda, m$	Lode angle related material parameters
c_η	stress triaxiality related material parameter

C_i	i= 1 to 6, material dependent parameters
D	damage evolution variable
d	local pipeline diameter
D_{CR}	critical damage
D_i	pipe's internal diameter
D_o	pipe's outer diameter
e	fluid specific internal energy
e_i	specific internal energy of liquid phase
e_v	specific internal energy of vapor phase
f_w	Fanning friction factor
G_f	dissipated energy
I_1, I_2, I_3	invariants of stress tensor
J_{CVN}	CVN fracture energy
J_{DWTT}	pre-cracked DWTT energy
K	strength coefficient
L	characteristic length
n	strain hardening exponent
P	fluid pressure
q_w	heat flux
T	temperature
U	total energy of the mixture per unit volume
u	fluid velocity
w_t	pipe's wall thickness
X	mass fraction of vapor phase

1. Introduction

Accurate and reliable prediction of fracture propagation in pipelines is of significant interest for safe design of pipelines transporting high-pressure fluids in various industries, including the process industry and nuclear and power generation. Therefore, estimation of fracture propagation is

an essential strategy to ensure pipeline integrity. However, dynamic fracture prediction is a challenging task, since it requires knowledge of the interaction between the dynamic forces driving crack growth and the resistance forces opposing fracture propagation. Moreover, numerous material properties should be taken into account.

Ductile fracture is typically characterized by wide crack flanks opening, relevant bulging at the crack tip and a large amount of plastic deformation in the vicinity of the flaps. Experimental burst tests reveal that the typical crack speed during ductile fracture propagation in steel pipelines is around 350 m/s [1]. Since the acoustic velocity of gas (such as lean gas or rich methane) under the usual operation conditions is in the range of 350–500 m/s, the decompression of the pipe is faster than the crack speed. This implies that the local pressure in the vicinity of the crack tip is lower than the initial pressure, and decreases with decreasing crack speed [2]. Therefore, a long running fracture occurs when the crack velocity exceeds the decompression wave velocity.

On the other hand, for environmental protection and safety reasons, a series of standardized materials tests, covering the entire range from small scale tensile tests up to full scale burst tests, should be performed under conditions of real applications. These tests involve a high volume of material and financial input for which reason the suppliers and constructors strive to substitute the greatest possible number of tests by using simulation techniques such as the Finite Element Modelling (FEM). In this way, specific testing conditions can be simulated, estimated and assessed prior to preparing an expensive test, in order to discover shortcomings in the design before performing a large scale test. To this end, computational fracture mechanics [3] is an emerging field of research with promising potential for pipeline design. While designers already rely on the FEM approach to predict structural stiffness and strength, vibro-acoustics, etc., pipeline engineering is still entirely based on experimental (and often large scale) testing and empirical proof of concept. Most pipe designers are reluctant to accept the benefits that numerical methods can bring, despite the fact that damage mechanics approaches for ductile fracture have been well documented in the literature [4].

In order to assess susceptibility of pipelines to crack propagation, semi-empirical methodologies such as the Battelle Two Curve (BTC) and High Strength Line Pipe (HLP) Committee methods have been proposed in the past. The BTC methodology involves comparison of the fluid decompression wave velocity with the crack velocity for a given pressure and specified pipeline

fracture toughness. A long running fracture is expected to occur if, at any time, the crack velocity exceeds the decompression wave velocity. However, one of the main drawbacks of the BTC approach is that it has been developed based on the assumption that the pipeline decompression and the fracture propagation phenomena are decoupled. Therefore, it is not possible to predict the variation of the crack length with crack propagation velocity. To this end, the crack arrest length, which is an important parameter in the design and spacing of crack arrestors, cannot be correctly estimated.

To predict more accurately the crack tip pressure variation during the pipeline decompression and resolve the crack propagation along the pipeline with the time, several authors have developed methodologies for coupling the pipeline outflow and crack propagation models [5-7]. These methodologies are largely based on Homogenous Equilibrium Mixture (HEM) model of pipeline decompression flow, and use different methods to account for a moving crack. In the present study, to estimate the history of pipeline decompression during pipeline ductile fracture more accurately, a fully coupled fluid/structure fracture model is developed. The proposed model allows the quantitative prediction of the pipeline propensity to long running fractures in the form of the variation of crack length with crack velocity and ultimately the crack arrest length.

More theoretically substantiated fracture models [8] describing the damage locally are potentially able to describe the failure of a material for different geometries and thicknesses. These models are based on the early computation of void growth according to Rice and Tracey [9], and account for the local softening of the material due to void growth and later coalescence. Furthermore, these models have been proven to correctly describe the mechanisms of damage at the local scale [10]. Several approaches can be pursued to model plastic deformation and ductile failure of metals. Bonora [11] developed a Continuum Damage Mechanics (CDM) model, where the growth of microvoids results in nonlinear damage accumulation with plastic deformation. Ductile crack growth analyses based on failure predictions of a porous plastic material model have been carried out by Needleman and Tvergaard [12]. The porous plasticity model is usually referenced to as the Gurson-Tvergaard-Needleman (GTN) model, initiated by the work of Gurson [13] and further developed by Tvergaard and Needleman [8, 14-16]. Bonora et al. [17] and Dunand and Mohr [18] have revealed that, when using GTN model, the prediction of the calibrated material parameters on geometries that were not involved in the calibration procedure has not been proven to be satisfactory.

6

It has been proven in the literature that the fracture strain is strongly dependent on stress triaxiality, defined as the ratio of pressure over the equivalent stress [9, 19-22]. Recent studies have shown that another parameter, Lode angle (related to the third invariant of the deviatoric stress tensor) also has a significant impact on the fracture strain [23-26]. These types of modelling approach have been used quite often in the pipeline industry for ductile fracture behavior of different steel grades [27-29]. Recently, Lian et al. [10] have modelled the plasticity and ductile fracture behavior of a dual-phase steel sheet by proposing a modified Bai-Wierzbicki (BW) damage model derived from the combination of different types of damage models. They have made some important modifications to the BW model, so that it is called the Modified Bai-Wierzbicki (MBW) model. Their modified model, i.e. MBW, addresses the effects of stress state on the plastic behavior and the onset of damage of materials, and quantifies the microstructure degradation using a dissipation-energy-based damage evolution law.

Novokshanov et al. [30] have extended the MBW, where they have included strain rate and temperature dependent plasticity and a ductile damage model for isotropic materials. The added correction functions were dependent on the second and third invariants of the stress deviator as well as the hydrostatic stress. To model the ductile running fracture in a pipeline, various approaches have been adapted, ranging from the HLP model [5] to more complex models where pipeline deformations and fracture are predicted using elasto-plastic models [31]. Recently, Hojjati-Talemi et al. [32] have applied a more theoretically-substantiated continuum material failure model [23] to predict more reliably and accurately the ductile crack propagation phenomena.

In the present study, a methodology for modelling running fracture in steel pipelines, coupling the pipeline outflow model with the fracture propagation model, i.e. Extended Modified Bai-Wierzbicki (XMBW), is developed. The coupled model is then compared with HLP model and validated against experimental data obtained from one of the full-scale burst tests performed by the British Gas Company (BGC) on line pipes made from API grade X70 steel, with an outer diameter of $D_o \approx$ 1.2m and 18.3mm wall thickness [33]. The following describes the main features of the proposed methodology, results of the model validation and conclusions of the present study.

2. Pipeline decompression model

2.1 Fluid-structure interaction modeling concept

Long running ductile fracture is a transient phenomenon, which involves dynamic coupling of the pipe wall fracture and the pipeline decompression. In particular, as a result of fracture propagation, the length of the generic un-fractured section of the pipeline decreases. In turn, as the pressure in the pipeline drops during the decompression, the driving force for the pipe wall deformations and fracture weakens, while speed of the fracture propagation reduces. In order to model this coupled behavior, the fluid/structure interaction concept is developed in the present study. This concept assumes that running pipeline fracture is a propagating mode of Full-Bore Rupture (FBR) of a pipe, which can be modelled as an expansion in the pipe cross-section area from the initial pipe cross-section area A_0 to an arbitrary large area A_f.

Figure 1, (a) and (b) show respectively (a) the schematic representation of the pipeline section with a fracture along its length, and (b) the corresponding variation in the effective cross-sectional area of the pipeline in the proposed fracture dynamics model. In the one-dimensional flow model, the pipe rupture is simulated as a continuous expansion in the pipe cross-sectional area, which happens over a short interval ∂Z. The fracture propagation is then modelled as motion of the expansion front at an instantaneous speed $\dot{a}$.

Figure 1 Schematic representation of the pipeline ductile fracture (a) and the corresponding variation of the effective area of the pipeline simulated in the model (b).

The fracture speed $\dot{a}$ is governed by the structural mechanic's model and serves as one of the coupling parameters of the fluid-structure interaction model. The other coupling parameters of the model include the bulk fluid pressure at the crack tip.

2.2 Pipeline flow model

To predict the pertinent fluid properties within the pipeline during its decompression resulting from puncture or FBR, the Computational Fluid Dynamics (CFD) model has been developed based on the HEM assumption [34]. This model accounts for all the important processes taking place during depressurization, including heat transfer, friction, expansion wave propagation and multi-phase

flow. The HEM assumption implies thermal and dynamic equilibrium between saturated liquid and vapor phases, and approximately neglects non- equilibrium and heterogeneous nature of the flow.

In order to model the fluid flow in a pipeline undergoing running fracture, the pipeline cross-sectional area is set as variable, changing from the initial area A_0 of the pipe to an arbitrary large value A_f at the position of the crack tip. A set of equations describing the HEM flow in a variable cross-section pipe includes the advection equation for the pipe cross-sectional area and the mass, momentum and energy conservation equations [35]:

$$\frac{\partial A}{\partial t} + \dot{a}\frac{\partial A}{\partial z} = 0 \tag{1}$$

$$\frac{\partial A\rho}{\partial t} + \frac{\partial A\rho u}{\partial z} = 0 \tag{2}$$

$$\frac{\partial A\rho u}{\partial t} + \frac{\partial A(\rho u^2 + P)}{\partial z} = P\frac{\partial A}{\partial z} - \frac{2f_w A\rho u^2}{d} \tag{3}$$

$$\frac{\partial AE}{\partial t} + \frac{\partial Au(E + P)}{\partial z} = P\frac{4Aq_w}{d} - \frac{2f_w A\rho u^3}{d} \tag{4}$$

where ρ, u and P are the fluid density, velocity and pressure, respectively, which are functions of time t and space z; d and A are respectively the local instantaneous pipeline diameter and cross-sectional area, q_w is the heat flux at the pipe wall, f_w is the Fanning friction factor calculated using the Chen's correlation [36], and U is the total energy of the mixture per unit volume:

$$U = \rho(e + 0.5u^2) \tag{5}$$

where e and ρ are respectively the specific internal energy and density of the fluid, calculated using PC-SAFT equation of state [37, 38]:

$$e = xe_v(1 - x)e_1 \tag{6}$$

$$\frac{1}{\rho} = \frac{x}{\rho_v} + \frac{1 - x}{\rho_1} \tag{7}$$

Here x is the mass fraction of the vapor phase, and the subscripts v and l refer to the vapor and liquid phases, respectively.

9

Equation (1) describes the advection of the pipeline expansion front at a speed $\dot{a}$, which is calculated using the fracture mechanics model described in next section. The shape of the expansion front is specified in the Lagrangian framework using a smooth function in the following form:

$$A = f(A_f, \Delta z_f) \qquad (8)$$

Where A_f and Δz_f are the effective area of the expanded pipe and the smoothing distance, respectively.

2.3 Initial and boundary conditions

The governing equations (1) – (4) of the flow model can be solved subject to initial and boundary conditions for the flow at either end of the pipeline. At the closed end, located at z= 0, the appropriate condition is, u= 0, as depicted in **Figure 1**(b). At the other end of the pipe, where the fracture propagation is initiated, i.e. z= l, where l is the total length of the pipeline, the fluid is exposed to the ambient pressure. Hence, a ghost cell [39] is utilized, in which $dp/dt = 0$. The method of characteristics is used to apply the above boundary conditions in the numerical solution methodology as described by Thompson [40]. The numerical solution of the set of quasi-linear hyperbolic equations (1) – (9) describing flow in a variable cross-section are pipe is performed using the Finite-Volume Method [39], which has been programed using a Fortran language. Details of the implementation of this method were previously described [41], and for brevity are not included in this paper.

3. Dynamic fracture models

3.1 HLP model

Several empirical models of crack propagation have been developed based on simplified models of pipeline decompression and experimental information about crack propagation. In this study in order to calculate the crack propagation speed and verify the developed CFD-XMBW model, the HLP Committee for the ISIJ (Iron and Steel Institute of Japan) method was used. The HLP model

is relatively simple algebraic model which is based on the correlation proposed by [42] According to this approach the crack speed can be calculated as:

$$\dot{a} = 0.67 \frac{\sigma_f}{\sqrt{J_{DWTT} / A_p}} \left(P / P_a - 1 \right)^{0.393} \tag{9}$$

where P_a is the crack arrest pressure defined as:

$$Pa = 0.382 \frac{w_t}{D_i} \sigma_f \times \cos^{-1} \left(\exp \left(-\frac{3.81 \times 10^7 [m^3 / N]}{\sqrt{D_i w_t}} \times \frac{J_{DWTT} / A_p}{\sigma_f^2} \right) \right) \tag{10}$$

In the above equations, w_t and D_i are respectively the pipe wall thickness and the pipe internal diameter in [mm], while A_p is the ligament area of the pre-cracked Drop Weight Tear Test (DWTT) specimen in [mm²], which is function of the pipe wall thickness, J_{DWTT} is the pre-cracked DWTT energy in [J] and σ_f is the material flow stress in [MPa], which are respectively defined as [42]:

$$A_p = 71.12 \, [mm] \, w_t \tag{11}$$

$$J_{DWTT} = 3.29 \, w_t^{1.5} J_{CVN}^{0.544} \tag{12}$$

where J_{CVN} is Charpy V-Notch (CVN) fracture energy. The material flow stress, σ_f, is defined as follows:

$$\sigma_f = 0.5 \left(\sigma_y + \sigma_{ult} \right) \tag{13}$$

where σ_y and σ_{ult} are respectively the yield stress and ultimate tensile stress of the pipeline material.

3.2 Ductile XMBW fracture model

According to the yield potentials of von Mises and Tresca, the actual amount of hydrostatic pressure should not affect the yielding point since the diameters of the 3D yielding surfaces do not change with the increasing hydrostatic pressure. However, it has already been proven that the influence of the hydrostatic pressure on the plastic behavior of materials is crucial. Lemaitre [43] and Johnson and Cook [44] have revealed that the pressure strongly affects the strain at which ductile fracture occurs in the specimen. Johnson and Cook [44] have concluded that the ductile

11

fracture is much more dependent on the state of hydrostatic pressure than on the strain rate and the temperature. Most recently, Bai and Wierzbicki [23] have introduced a new model to describe plasticity and fracture of metals numerically. Their model considers not only the influence of the material's specific hardening behavior but also the influence of all three stress tensor invariants on plastic yielding, and hence respects the hydrostatic pressure and the Lode angle. The deviatoric stress tensor, σ'_{ij}, can be written as follows:

$$\sigma'_{ij} = \sigma_{ij} - \sigma_m \delta_{ij} \tag{14}$$

where σ_{ij} is the stress tensor, δ_{ij} is the Kronecker delta and σ_m is the mean stress. The three invariants of stress tensor are given by:

$$I_1 = -\sigma_m = -\frac{1}{3}\delta_{ij}\sigma_{kk} \tag{15}$$

$$I_2 = \bar{\sigma} = \frac{1}{2}\left[\sigma_{kk}^2 - \sigma_{ij}\sigma_{ij}\right] \tag{16}$$

$$I_3 = \varepsilon_{ijk}\sigma_{i1}\sigma_{j1}\sigma_{k1} \tag{17}$$

Therefore, stress triaxiality and Lode angle can be written as follows:

$$\eta = \frac{-I_1}{I_2} = \frac{\sigma_m}{\bar{\sigma}} \tag{18}$$

$$\theta = \frac{1}{3}\cos^{-1}\left[\left(\frac{I_3}{I_2}\right)^3\right] \tag{19}$$

The Lode angle θ is defined using the normalized third stress tensor invariant ξ:

$$\xi = \left(\frac{I_3}{I_2}\right)^3 = \cos(3\theta) \tag{20}$$

By normalizing the Lode angle, the Lode angle parameter can be expressed by

$$\bar{\theta} = 1 - \frac{6\theta}{\pi} = 1 - \frac{2}{\pi}\cos^{-1}(\xi), \ -1 \leq \bar{\theta} \leq 1 \tag{21}$$

Referring to the three-dimensional space, given by the three principal stresses σ_1, σ_2 and σ_3 and the hydrostatic pressure as the space diagonal, the actual stress state can be defined by using a polar coordinate system. Bai and Wierzbicki [23] postulated a yield function to calculate the yield stress as a function of the strain history, the stress triaxiality and the normalized Lode angle. Following Lian et al. [10] and Novokshanov et al. [30], the pressure dependency is neglected in this study, and the Lode-angle influence coupled with an isotropic hardening law is included in the yield criterion. The yield potential function (Φ) can be written as below:

$$\Phi = \sigma_{eq} - \sigma_y(1-D) \le 0 \tag{22}$$

where σ_{eq} is the equivalent stress and D is the damage evolution variable, which is elaborated later on. The flow curve $\bar{\sigma}(\bar{\varepsilon}_p)$, which is derived from a reference test of the considered material, gives the yield strength σ_y with respect to five correction terms. The initial implemented model by Lian et al. [10] only considered the effects of strain and stress states, whereas the extended model by Novokshanov et al. [30] has also taken into account the temperature and the strain rate influences. These effects have been added in an empirical way rather than in a physical one following the same approach by Johnson-Cook [44]. The XMBW model can be written as follows:

$$\sigma_y = \bar{\sigma}(\bar{\varepsilon}_p, \dot{\bar{\varepsilon}}_p) f(\eta, \bar{\theta}) f(T) \tag{23}$$

where $\bar{\sigma}(\bar{\varepsilon}_p, \dot{\bar{\varepsilon}}_p)$, $f(\eta, \bar{\theta})$ and $f(T)$ are correction functions for strain rate, stress state and temperature independent of each other. Eventually, all correction functions and the damage initiation and evolution variable D can be divided into the yield potential function (Φ) [30]:

$$\Phi = \sigma_{eq} - \underbrace{\left[\bar{\sigma}(\bar{\varepsilon}_p)\left(c_{\dot{\bar{\varepsilon}}}^1 \cdot \ln \dot{\bar{\varepsilon}}_p + c_{\dot{\bar{\varepsilon}}}^2 \cdot \dot{\bar{\varepsilon}}_p\right) + c_{\dot{\bar{\varepsilon}}}^3 \cdot \dot{\bar{\varepsilon}}_p\right]}_{\bar{\sigma}(\bar{\varepsilon}_p, \dot{\bar{\varepsilon}}_p)} \times \underbrace{\left[c_T^1 \cdot \exp\left(-c_T^2 \cdot T\right) + c_T^3\right]}_{f(T)}$$

$$\times \underbrace{\left[1 - c_\eta \cdot (\eta - \eta_0)\right] \times \left[c_\theta^s + \left(c_\theta^{ax} - c_\theta^s\right)\left(\lambda - \frac{\lambda^{m+1}}{m+1}\right)\right]}_{f(\eta, \bar{\theta})}(1-D) \le 0 \tag{24}$$

where

$$\bar{\sigma}(\bar{\varepsilon}_p, \dot{\bar{\varepsilon}}_p) = \bar{\sigma}(\bar{\varepsilon}_p)\left(c_{\dot{\bar{\varepsilon}}}^1 \cdot \ln \dot{\bar{\varepsilon}}_p + c_{\dot{\bar{\varepsilon}}}^2 \cdot \dot{\bar{\varepsilon}}_p\right) + c_{\dot{\bar{\varepsilon}}}^3 \cdot \dot{\bar{\varepsilon}}_p \tag{25}$$

$$f(T) = \left[c_T^1 . \exp\left(-c_T^2 . T\right) + c_T^3 \right] \tag{26}$$

$$f(\eta, \bar{\theta}) = \left[1 - c_\eta . (\eta - \eta_0)\right] \left[c_\theta^s + \left(c_\theta^{ax} - c_\theta^s\right) \left(\lambda - \frac{\lambda^{m+1}}{m+1} \right) \right] \tag{27}$$

with λ and c_θ^{ax} defined as follows:

$$\lambda = \frac{\cos(\pi/6)}{1 - \cos(\pi/6)} \left(\frac{1}{\cos(\theta - \pi/6)} - 1 \right) \tag{28}$$

$$c_\theta^{ax} = \begin{cases} c_\theta^t & \bar{\theta} \geq 0 \\ c_\theta^c & \bar{\theta} < 0 \end{cases} \tag{29}$$

The reference flow curve can be determined at the reference temperature and the reference strain. $c_{\dot{\varepsilon}}^1, c_{\dot{\varepsilon}}^2$ and $c_{\dot{\varepsilon}}^3$ are strain rate material parameters, c_T^1, c_T^2 and c_T^3 are temperature dependent material parameters and the constants $c_\eta, c_\theta^t, c_\theta^s, c_\theta^c$ and m are stress state material parameters. Following the works by Lian et al. [10] and Novokshanov et al. [30], a locally coupled damage evolution law is applied in this study that clearly differentiates between macroscopic fracture and microscopic crack initiation. Generally ductile fracture is driven by the formation, the growth and the coalescence of voids on the microscopic scale. The coalescence of voids as the last microscopic step is defined as the micro-crack initiation.

In a material underlying a proceeding damage evolution, Lemaitre [43] defines the damage variable D to represent the decrease in the residual cross-section area to carry the induced stress. The general approach, which related the fracture strain to the stress triaxiality, had already been published by Lemaitre [43] and Johnson and Cook [44]. The damage variable D can be written as follows:

$$D(\bar{\varepsilon}_p) = \int_0^{\bar{\varepsilon}_p} \frac{d\bar{\varepsilon}_p}{f(\eta, \bar{\theta})} \tag{30}$$

The mathematical description of the 3D fracture locus by Bai and Wierzbicki [23] is expressed as:

$$\hat{\varepsilon}_f(\eta, \bar{\theta}) = \left[\frac{1}{2}(C_1 e^{-C_2 \eta} + C_5 e^{-C_6 \eta}) - C_3 e^{-C_4 \eta} \right] \bar{\theta}^2 + \frac{1}{2}(C_1 e^{-C_2 \eta} + C_5 e^{-C_5 \eta}) \bar{\theta}^2 + C_3 e^{-C_4 \eta} \tag{31}$$

The constants C_1 to C_6 are material dependent and need to be determined. After Lian et al. [10] the onset of ductile plastic deformation is not imperatively the point of damage initiation, which more often shows up after a certain amount of plastic deformation has already occurred. Both Lian et al. [10] and Novokshanov et al. [30] have described the microscopic ductile damaging behavior of API X70 pipeline steel using a 3D damage initiation locus $\hat{\varepsilon}_i(\eta,\bar{\theta})$ to predict the micro-crack initiation. The 3D fracture locus $\hat{\varepsilon}_f(\eta,\bar{\theta})$ represents the macroscopic damaging behavior. The symmetric shape with respect to the Lode angle is used due to a simpler handling while still achieving a satisfying accuracy. The mathematical description of this 3D damage initiation locus with the reduction to only the four remaining material constants C_1 to C_4 is given by:

$$\hat{\varepsilon}_i(\eta,\bar{\theta}) = \left[C_1 e^{-C_2\eta} - C_3 e^{-C_4\eta}\right]\bar{\theta}^2 + C_3 e^{-C_4\eta} \tag{32}$$

After the equivalent plastic strain of crack initiation $\hat{\varepsilon}_i$ is reached, the damage variable D increases according to the dissipation-energy-based damage evolution law expressed as:

$$\dot{D} = \frac{\sigma_y^i L}{2 G_f} \dot{\bar{\varepsilon}}_p \tag{33}$$

where L is the characteristic length associated to an integration point in the simulation, σ_y^i is the yield strength at onset of damage, $\dot{\bar{\varepsilon}}_p$ is the equivalent plastic strain rate and G_f is the required dissipated energy to advance a crack by a certain surface unit area. The dissipation energy G_f represents the resistance of a material against crack growth by influencing the slope of the damage variable evolution. The damage evolution law can be written as follows:

$$D = \begin{cases} 0 & \bar{\varepsilon} \leq \bar{\varepsilon}_i \\ \int_{\bar{\varepsilon}_i}^{\varepsilon} \frac{\sigma_y^i}{2 G_f} d\bar{\varepsilon} & \bar{\varepsilon}_i < \bar{\varepsilon} < \bar{\varepsilon}_i \\ D_{cr} & \bar{\varepsilon} = \bar{\varepsilon}_f \end{cases} \tag{34}$$

For more information regarding to yield potential function and damage evolution law, readers are referred to studies published by Lian et al. [10], Novokshanov et al. [30] and Hojjati-Talemi et al. [32].

4. Fluid-structure coupling algorithm

A theoretically substantiated approach is applied to simulate the ductile fracture propagation in steel pipeline, where the material damage is resolved using a ductile fracture mechanics model. The coupling of CFD outflow and fracture model is based on a feedback algorithm. The first step involves the computations of the bulk fluid pressure at the crack tip and the corresponding crack tip pressure for an arbitrary small initial longitudinal crack opening along the major axis of the pipeline, formed for example, as a result of the third party damage. In the CFD model, the crack tip is defined as the point where the pipe area expands by 10%. To achieve the dynamic coupling of fracture and outflow models, an explicit time integration scheme is applied.

The corresponding crack tip velocity is then calculated using the fracture models described in Section 3, i.e. both HLP and XMBW. A zero crack velocity means no propagation and the calculations are terminated. For a positive value, on the other hand, the new crack opening area is determined after an arbitrary small time increment, Δt (=0.001 s). Based on the new crack opening area and time interval, the mass of fluid escaping and hence the new crack tip pressure are calculated using the fluid flow model described in Section 2. This procedure is repeated for further time increments until the crack velocity reaches zero.

5. Material parameters

The implemented XMBW model consists of 17 material parameters that need to be determined in order to predict the behavior of a material with a satisfactory accuracy. API X70 pipeline steel is used in this investigation with a minimum 485MPa yield strength and a minimum 570MPa tensile strength. This material is a micro-alloyed high-strength steel grade, which got thermo mechanically rolled, it consists of a ferritic matrix with a certain pearlitic content. The chemical and mechanical properties of steel are highly dependent on the alloying concept. The right choice of this alloying concept appropriates the steel for its later application. The chemical composition of the steel X70 is tabulated in **Table 1**. Quasi static round bar tensile tests were performed at room temperature to determine the mechanical properties of the X70 steel. Mechanical properties of API X70 steel are listed in **Table 2**. Moreover, the flow curve of the material was calculated from the experimental

16

results. Thereafter, it was fitted using Ludwik's strain hardening equation and extrapolated to large plastic strain as:

$$\overline{\sigma}(\overline{\varepsilon}_p) = \sigma_y + k\,\overline{\varepsilon}_p^{\,n} \tag{35}$$

where K is the strength coefficient and n is the strain hardening exponent.

Table 1 Chemical composition of the X70, mass contents in percentage

Table 2 Tensile properties of the pipeline steel X70

The material constants of Equation (24) can be divided in different groups, namely strain rate correction factors, stress state parameters, temperature correction parameters and damage evolution constants. To calibrate the 17 material parameters for the XMBW model, four experimental set-ups could be used. The experimental program relies on tensile tests on shear samples, flat grooved plane strain samples and notched cylindrical bars as well as on upsetting tests on notched compression samples. To cover a wide range of stress states, different notch radii should be used for these samples. More information about the material calibration process can be found in the literature [30]. **Table 3** shows the calibrated material parameters for X70 pipeline steel grade, obtained in a previous study [32].

Table 3 The XMBW model material parameters for the X70 steel.

6. Numerical simulation

In order to validate the developed XMBW model, dynamic impact tests, i.e. CVN and DWTT, are modeled using the finite element simulation. Furthermore, as is mentioned above, to validate the coupled fluid-structure model, simulations are performed for conditions of the ductile fracture propagation of the full-scale burst test performed by the British Gas Company (BGC) on line pipes made from API grade X70 steel [33]. All simulations are performed in ABAQUS/Explicit with the strain rate and temperature dependent VUMAT subroutine implementation of the XMBW model.

6.1 CVN model

In this study, the CVN impact test configuration is modelled using ABAQUS. The CVN specimen's dimensions are $10{\times}10{\times}55$ mm^3 according to the ASTM E23 standard [45]. The model

consists of four parts, namely a hammer, two anvils and the CVN specimen which can be meshed independently. **Figure 2** illustrates the finite element mesh of the specimen, an assembled view and loading conditions of the CVN model.

A three-dimensional eight-node linear hexahedral continuum element (C3D8R) is used in order to mesh the experimental configuration. A mesh size of $0.15 \times 0.15 \times 0.15$ mm^3 is considered at the potential crack propagation regions and increased gradually away from the area of interest. Moreover, to capture correctly the multiaxial stress gradient at the notch tip, the mesh size is decreased to 0.05mm. Rigid parts are used to represent the anvils and the hammer. The anvils are defined to remain immobile whereas the striker can only move parallel to the Y-axis. Due to the use of predefined fields, the striker has an initial velocity of 5.5m/s and a constant mass of 19.81kg.

Contact is considered between the hammer and the specimen, as well as between the specimen and the anvils assuming a Coulomb friction law with a friction coefficient of 0.1. The contact between the hammer and the specimen along with the anvils and the specimen is defined using the master–slave algorithm in ABAQUS for contact between two surfaces. The surfaces of the hammer and the anvils are defined as slave surface, and the surface of the specimen is defined as a master surface. Loading is modelled by prescribing the initial velocity of the hammer.

Figure 2 Three-dimensional meshing of the CVN specimen along with applied loading and boundary conditions.

6.2 DWTT model

The DWTT model is created with a sample size of 305mm length, 76.2mm height and the original thickness of the used steel plate (in this case 16mm), as is depicted in **Figure 3**. The anvils and the drop-hammer have been modelled as rigid bodies. The contact properties between the hammer and the DWTT specimen as well as between the anvils and the DWTT specimen have been defined the same as for the CVN model with a friction coefficient of 0.1. The mass of the hammer is set to 690kg and the initial impact velocity to 6.5m/s. These values were chosen according to the experiments which were performed according to API RP 5L3 standard. Meshing is optimized by using a finer mesh in the region of the fracture surface. The mesh size is defined by the smallest elements to 0.1mm³.

Figure 3 Finite element model of the DWTT specimen.

6.3 Fluid-structure fracture simulation

In order to validate the coupled fluid-structure fracture model, the numerical results are compared with the results of one of the full-scale burst test of a buried pipeline. In the test selected for the model validation, the natural gas was pressurized till 11.6MPa. This full scale test involved rupture of an X70 grade steel pipeline, of 50m in length, an outer diameter of ≈1.2m and 18.3mm wall thickness. Prior to the rupture, the pipeline was filled with rich natural gas (containing ca 89.55 % (v/v) of methane) compressed to 11.6 MPa at –5 °C.

Figure 4 illustrates the finite element mesh used in ABAQUS simulations of the full-scale burst test. A major advantage in the case of running ductile fracture is that the path of crack propagation is well-known. Therefore, only one quarter of the full scale experimental tests is modelled due to double symmetry conditions with respect to X-Y and Y-Z planes. The physical issue of crack initiation is not of relevance for prolonged release experiments. The fracture scenario is focused on an already existing through-wall crack advancing in longitudinal pipe direction, similar to the experimental test situation. As is depicted in the figure, the initial crack length is selected to be one time the outer pipe diameter, promoting pipe opening and initial crack propagation. The crack propagation section is covered by the XMBW fracture model. The pipe end is fully constrained over a length of one time the outer diameter. This closed end section is required as otherwise the crack velocity starts to accelerate randomly towards the end of the pipe.

A three-dimensional eight-node linear hexahedral continuum element (C3D8R) is used in order to model the experimental configuration. The minimum mesh size along the crack propagation path is 6mm and increased gradually away from the area of interest. The applied analysis procedure is "explicit dynamic" which also includes mass inertia effects. The global depressurization is modelled using the fluid-structure coupling method as is elaborated above. The fluid-structure interaction coupling time step of 0.1ms is chosen to guarantee convergence of the results when using CFD grids with resolution of 10-15cells/m.

For any finite element simulation of crack propagation, the damage model links local physical material behavior with global component failure. It is essential to define the damage response of material at the ultimate state of stress. However, the material constants have to be calibrated using

small scale laboratory testing as is explained above. Furthermore, as long as the involved dissipated fracture energy is quantified properly by the damage model, the morphology of the fracture surface is not of any relevance. Concerning accuracy of crack length prediction, it is typical not about millimeters, mostly not even centimeters of ductile crack growth, but rather on a decimeter scale. To this end, only one element is used through the thickness of pipe to reduce the computation time.

Figure 4 Finite element mesh of prolonged release experiment.

During crack propagation in a pipe, pipe wall opens in the radial direction behind the crack front, which is called flap opening as is indicated schematically in Figure 4. When a pipe is buried in soil, which is the case in this study, the driving force for crack propagation is constrained. It follows that a crack becomes less likely to propagate long in a pipeline with soil backfill pressure. This effect is called the soil backfill effect, which increases the resistance against propagation. There are different ways to model the backfill effect [42], which is out of the scope of this study. Nevertheless, in a simplified approach, it is possible to apply an external pressure on the outer surface of the pipe to simulate the effect of backfill pressure of the soil. Therefore, a constant external pressure of 5 MPa is applied on the outer surface of the pipe during running fracture as was suggested by Makino et al. [42].

7.   Result and discussion

7.1 Fracture simulation results of CVN and DWTT

Figure 5 depicts the comparison of force against hammer displacement between simulation result and experimental observation for the CVN sample. As can be seen from the figure, the predicted results of the XMBW fracture model show good correlation with the experimental observations. **Figure 6** compares the force against displacement curves from experiment and simulation for DWTT sample. Like for the CVN sample, the developed XMBW fracture model can reproduce the ductile fracture behavior of X70 steel pipeline of the DWTT sample when subjected to dynamic loading conditions. The obtained results confirm the fact that the developed fracture model can estimate the dynamic ductile fracture correctly. Next step is then coupling the CFD model with the XMBW model to reproduce the ductile fracture of the prolonged release experiment, as is elaborated in next section.

Figure 5 Comparison of the results of simulation with experimental observation of CVN sample.

Figure 6 Load vs. displacement curve from BDWT test on X70 steel grade at T = 23°C. Experimental results and numerical results derived with the extended MBW model.

7.2 Fracture simulation results of the prolonged release experiment

Figure 7 shows the deformed shape of the pipeline as is predicted by the coupled fluid-structure interaction model, i.e. FCD+XMBW model, at different times. It can be seen that, following the fracture propagation, the wall of the unzipped section of the pipe becomes corrugated, which can be attributed to the plastic deformations of the pipe during the fracture. Remarkably, the shape of the fractured pipe predicted by the model is in a qualitative agreement with the shape observed in a real burst test. Although the main advantage of the CFD+XMBW model is its capability to predict in detail the ductile fracture for a structure of arbitrary geometry.

Figure 8 (a) and (b) shows the variation of the crack driving stress component (σ_{xx}) along the crack path and the flap opening of the fractured pipe at the different crack propagation time steps, respectively.

Figure 7 Corrugated shape of the pipe wall predicted by XMBW model during ductile fracture propagating at 0.1s after the initiation of the crack propagation.

Figure 8 (a) Variation of stress component σ_{xx} along the crack path and (b) flap opening of fractured pipe during ductile crack propagation steps.

Figure 9 illustrates a schematic view of the crack propagation velocity against the traveled distance along a pipe as has been reported by Civallero et al. [46]. The crack propagation in a steel pipeline normally follows three stages as is shown in **Figure 9**. A starting phase during which the crack reaches its maximum speed, a stationary crack advancing phase in which the crack speed is almost constant, and finally the crack arrest phase. It is worth mentioning that the experimental data, taken from the literature, were recorded only during the second phase of crack propagation. Therefore, the estimated numerical results were compared against the experimental observations only during the second stage.

Figure 10 shows the estimated crack tip velocity variation along the pipeline using the developed CFD+XMBW and FCD+HLP models which are compared with the observed experimental data taken from the literature [33]. At crack lengths lower than *ca.* 10m, i.e. at the beginning of the crack propagation, both the models overestimate the crack tip velocity, especially when using the coupled (XMBW+CFD) model. However, at crack lengths between 10 and 20m, both the CFD+XMBW and the CFD+HLP models predict the crack velocities around 150m/s, independent of the number of discretization cells for CFD+XMBW model, and in a good agreement with the observed experimental data. It can be noted that the CFD+HLP model estimates the crack arrest length of *ca.* 21m, while the XMBW+CFD model, for both CFD mesh resolutions, i.e. 500 and 750 cells, estimates the crack arrest length around 24m, which is close to the estimated crack arrest length as has been reported by Inoue et al. [33].

Figure 9 Schematic view of crack propagation velocity versus traveled distance [46]

Figure 10 Variation of the crack propagation speed with the crack length as predicted by the empirical HLP and XMBW models in comparison with the experimental data from Inoue et al. [33] at 0.2s after the initiation of the crack propagation.

8. Conclusion

In this research study, a methodology is described for coupled modelling of an outflow and crack propagation in steel pipelines. The main constituent elements of the methodology include the transient dynamically-coupled fluid-structure interaction model of pipeline fracture propagation. The proposed methodology couples the CFD model describing the pipeline decompression, and the XMBW fracture model, which has been implemented in the FEA code ABAQUS. The coupled fluid-structure ductile fracture model has been validated against experimental data reported in the literature on fracture propagation in a large-scale X70 pipeline. The study leads to the following conclusions:

- In order to accurately model the ductile fracture propagation in pipeline steels, accounting for the effects of stress sate, temperature, strain hardening and damage evolution, the XMBW model can be used. This model consists of 17 material parameters, which should be calibrated through several material tests performed for different steel grades and material failure conditions.

- For validating the developed XMBW fracture model, the CVN and the DWTT tests were simulated. The obtained estimated results show that using carefully calibrated set of the XMBW model parameters allows an accurate prediction of the ductile fracture of the X70 steel under dynamic loading conditions.

- The coupled fluid-structure interaction model (i.e. CFD+XMBW model) has been applied to simulate a full-scale burst test from the literature, showing that the coupled approach is capable of predicting the real fracture behavior of pipeline steels under different dynamic loading conditions relevant to running fractures in real-scale high-pressure pipelines. Moreover, the obtained numerical results using the CFD+XMBW model have also been compared with the CFD+HLP model, showing that the CFD+HLP fracture model underestimates the crack arrest length.

Acknowledgement

References

[1] G. Demofonti, G. Mannucci, M. Di Biagio, H. Hillenbrand, and D. Harris, "Fracture propagation resistance evaluation of X100 TMCP steel pipes for high pressure gas transportation pipelines using full-scale burst tests," in *4th Internal Conference on Pipeline Technology, Ostend, Belgium*, 2004, pp. 467-482.

[2] P Thibaux and F Van den Abeele, "Determination of crack initiation and propagation energy in instrumented Charpy V-notch impact tests by finite element simulations," presented at the Pipeline Technology Conference, Ostend, Belgium, 2009.

[3] M. H. Aliabadi and D. P. Rooke, *Numerical fracture mechanics*. Springer Science & Business Media, 1991.

[4] J. Besson, "Continuum models of ductile fracture: a review," *International Journal of Damage Mechanics,* 2009.

[5] H. Mahgerefteh, S. Brown, and G. Denton, "Modelling the impact of stream impurities on ductile fractures in CO_2 pipelines," *Chemical Engineering Science,* vol. 74, pp. 200-210, 2012.

[6] P. Aursand, M. Hammer, S. T. Munkejord, and Ø. Wilhelmsen, "Pipeline transport of CO2 mixtures: Models for transient simulation," *International Journal of Greenhouse Gas Control,* vol. 15, pp. 174-185, 2013.

[7] E. Aursand, C. Dørum, M. Hammer, A. Morin, S. T. Munkejord, and H. O. Nordhagen, "CO2 pipeline integrity: Comparison of a coupled fluid-structure model and uncoupled two-curve methods," *Energy Procedia,* vol. 51, pp. 382-391, 2014.

[8] V. Tvergaard, "Material failure by void growth to coalescence," *Advances in applied Mechanics,* vol. 27, no. 1, pp. 83-151, 1990.

[9] J. R. Rice and D. M. Tracey, "On the ductile enlargement of voids in triaxial stress fields," *Journal of the Mechanics and Physics of Solids,* vol. 17, no. 3, pp. 201-217, 1969.

[10] J. Lian, M. Sharaf, F. Archie, and S. Münstermann, "A hybrid approach for modelling of plasticity and failure behaviour of advanced high-strength steel sheets," *International Journal of Damage Mechanics,* vol. 22, no. 2, pp. 188-218, 2013.

[11] N. Bonora, "A nonlinear CDM model for ductile failure," *Engineering Fracture Mechanics,* vol. 58, no. 1, pp. 11-28, 1997.

[12] A. Needleman and V. Tvergaard, "An analysis of ductile rupture modes at a crack tip," *Journal of the Mechanics and Physics of Solids,* vol. 35, no. 2, pp. 151-183, 1987.

[13] A. L. Gurson, "Continuum theory of ductile rupture by void nucleation and growth: Part I—Yield criteria and flow rules for porous ductile media," *Journal of engineering materials and technology,* vol. 99, no. 1, pp. 2-15, 1977.

[14] V. Tvergaard, "Influence of voids on shear band instabilities under plane strain conditions," *International Journal of Fracture,* vol. 17, no. 4, pp. 389-407, 1981.

[15] V. Tvergaard, "On localization in ductile materials containing spherical voids," *International Journal of Fracture,* vol. 18, no. 4, pp. 237-252, 1982.

[16] V. Tvergaard and A. Needleman, "Analysis of the Charpy V-notch test for welds," *Engineering Fracture Mechanics,* vol. 65, no. 6, pp. 627-643, 2000.

[17] N. Bonora, D. Gentile, A. Pirondi, and G. Newaz, "Ductile damage evolution under triaxial state of stress: theory and experiments," *International Journal of Plasticity,* vol. 21, no. 5, pp. 981-1007, 2005.

[18] M. Dunand and D. Mohr, "Hybrid experimental–numerical analysis of basic ductile fracture experiments for sheet metals," *International Journal of solids and structures,* vol. 47, no. 9, pp. 1130-1143, 2010.

[19] F. A. McClintock, "A criterion for ductile fracture by the growth of holes," *Journal of applied mechanics,* vol. 35, no. 2, pp. 363-371, 1968.

[20] Y. Bao and T. Wierzbicki, "On fracture locus in the equivalent strain and stress triaxiality space," *International Journal of Mechanical Sciences,* vol. 46, no. 1, pp. 81-98, 2004.

[21] A. Mackenzie, J. Hancock, and D. Brown, "On the influence of state of stress on ductile failure initiation in high strength steels," *Engineering Fracture Mechanics,* vol. 9, no. 1, pp. 167-188, 1977.

[22] M. Mirza, D. Barton, and P. Church, "The effect of stress triaxiality and strain-rate on the fracture characteristics of ductile metals," *Journal of materials science,* vol. 31, no. 2, pp. 453-461, 1996.

[23] Y. Bai and T. Wierzbicki, "A new model of metal plasticity and fracture with pressure and Lode dependence," *International Journal of Plasticity,* vol. 24, no. 6, pp. 1071-1096, 2008.

[24] I. Barsoum and J. Faleskog, "Rupture mechanisms in combined tension and shear—experiments," *International Journal of solids and structures,* vol. 44, no. 6, pp. 1768-1786, 2007.

[25] X. Gao, G. Zhang, and C. Roe, "A study on the effect of the stress state on ductile fracture," *International Journal of Damage Mechanics,* 2009.

[26] G. Mirone and D. Corallo, "A local viewpoint for evaluating the influence of stress triaxiality and Lode angle on ductile failure and hardening," *International Journal of Plasticity,* vol. 26, no. 3, pp. 348-371, 2010.

[27] C.-K. Oh, Y.-J. Kim, J.-H. Baek, Y.-P. Kim, and W. Kim, "A phenomenological model of ductile fracture for API X65 steel," *International Journal of Mechanical Sciences,* vol. 49, no. 12, pp. 1399-1412, 2007.

[28] K. Kofiani, A. Nonn, and T. Wierzbicki, "New calibration method for high and low triaxiality and validation on SENT specimens of API X70," *International Journal of Pressure Vessels and Piping,* vol. 111, pp. 187-201, 2013.

[29] A. Keshavarz, R. Ghajar, and G. Mirone, "A new experimental failure model based on triaxiality factor and Lode angle for X-100 pipeline steel," *International Journal of Mechanical Sciences,* vol. 80, pp. 175-182, 2014.

[30] B. D. Denis Novokshanov, Mohamed Sharaf, Sebastian Münstermann, Junhe Lian, "A new model for metal toughness assessment with a computationally efficient parameter identification algorithm," *Engineering Fracture Mechanics,* 2015.

[31] H. O. Nordhagen, S. Kragset, T. Berstad, A. Morin, C. Dørum, and S. T. Munkejord, "A new coupled fluid–structure modeling methodology for running ductile fracture," *Computers & Structures,* vol. 94–95, pp. 13-21, 3// 2012.

[32] R. Hojjati, M. Steinhoff, S. Cooreman, F. Van den Abeele, and P. Verleysen, "Effects of High Strain Rates on Ductile Slant Fracture Behaviour of Pipeline Steel: Experiments and Modelling," in *2016 11th International Pipeline Conference,* 2016, pp. V003T05A010-V003T05A010: American Society of Mechanical Engineers.

[33] T. Inoue, H. Makino, S. Endo, T. Kubo, and T. Matsumoto, "Simulation method for shear fracture propagation in natural gas transmission pipelines," in *The Thirteenth International Offshore and Polar Engineering Conference*, 2003: International Society of Offshore and Polar Engineers.

[34] H. Mahgerefteh, P. Saha, and I. G. Economou, "Fast numerical simulation for full bore rupture of pressurized pipelines," *AIChE journal,* vol. 45, no. 6, pp. 1191-1201, 1999.

[35] M. J. Zucrow and J. D. Hoffman, "Gas dynamics," *New York: Wiley, 1976,* 1976.

[36] N. H. Chen, "An explicit equation for friction factor in pipe," *Industrial & Engineering Chemistry Fundamentals,* vol. 18, no. 3, pp. 296-297, 1979.

[37] N. I. Diamantonis, G. C. Boulougouris, E. Mansoor, D. M. Tsangaris, and I. G. Economou, "Evaluation of cubic, SAFT, and PC-SAFT equations of state for the vapor–liquid equilibrium modeling of CO2 mixtures with other gases," *Industrial & Engineering Chemistry Research,* vol. 52, no. 10, pp. 3933-3942, 2013.

[38] S. Brown *et al.*, "Thermodynamic interpolation for the simulation of two-phase flow of non-ideal mixtures," *Computers & Chemical Engineering,* vol. 95, pp. 49-57, 2016.

[39] R. J. LeVeque, *Finite volume methods for hyperbolic problems*. Cambridge university press, 2002.

[40] K. W. Thompson, "Time dependent boundary conditions for hyperbolic systems," *Journal of computational physics,* vol. 68, no. 1, pp. 1-24, 1987.

[41] S. Brown, S. Martynov, H. Mahgerefteh, and C. Proust, "A homogeneous relaxation flow model for the full bore rupture of dense phase CO2 pipelines," *International Journal of Greenhouse Gas Control,* vol. 17, pp. 349-356, 2013.

[42] H. Makino *et al.*, "Natural gas decompression behavior in high pressure pipelines," *ISIJ international,* vol. 41, no. 4, pp. 389-395, 2001.

[43] J. Lemaitre, "How to use damage mechanics," (in English), *Nuclear Engineering and Design,* Article vol. 80, no. 2, pp. 233-245, 1984.

[44] G. R. Johnson and W. H. Cook, "Fracture characteristics of three metals subjected to various strains, strain rates, temperatures and pressures," *Engineering Fracture Mechanics,* vol. 21, no. 1, pp. 31-48, 1985.

[45] *Standard test methods for notched bar impact testing of metallic materials*, 2007.

[46] M. Civallero, M. Mirabile, and G. Sih, "Fracture mechanics in pipeline technology," *Analytical and Experimental Fracture Mechanics, ed. Sih, GC and Mirabile, M,* pp. 157-174, 1981.

Table 1

C	Si	Mn	P	S	Cr	Ti	Al	V	Nb
0.064	0.37	1.8	0.012	0.001	0.011	0.023	0.037	0.005	0.081

Table 2

E [GPa]	σ_y [MPa]	σ_{ult} [MPa]	K [-]	n [-]
210	520	650	473	0.3023

Table 3

Strain Rate Correction Factors		
$c_{\bar{\varepsilon}}^1$	$c_{\bar{\varepsilon}}^2$	$c_{\bar{\varepsilon}}^3$
0.0071	0.015093	0.015075

Stress State Parameters				
c	c^t	c^s	c^c	m
0	0.9	1	1	4

Temperature Correction Parameters		
c_T^1	c_T^2	c_T^3
1.34	0.01	0.95

Damage Evolution Constants					
c_1	c_2	c_3	c_4	G_f	D_{cr}
0.037	0.949	0.005	2.303	4000	0.15

Figure 1 (single column image = 90mm width)
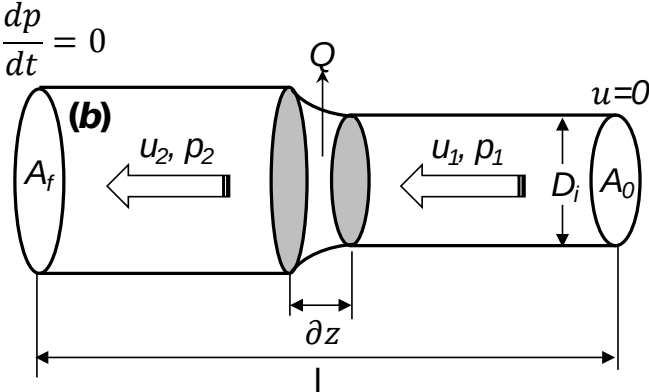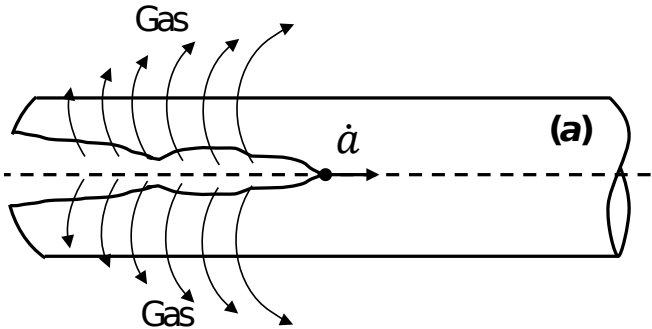
Figure 2 (double column image = 140mm width)
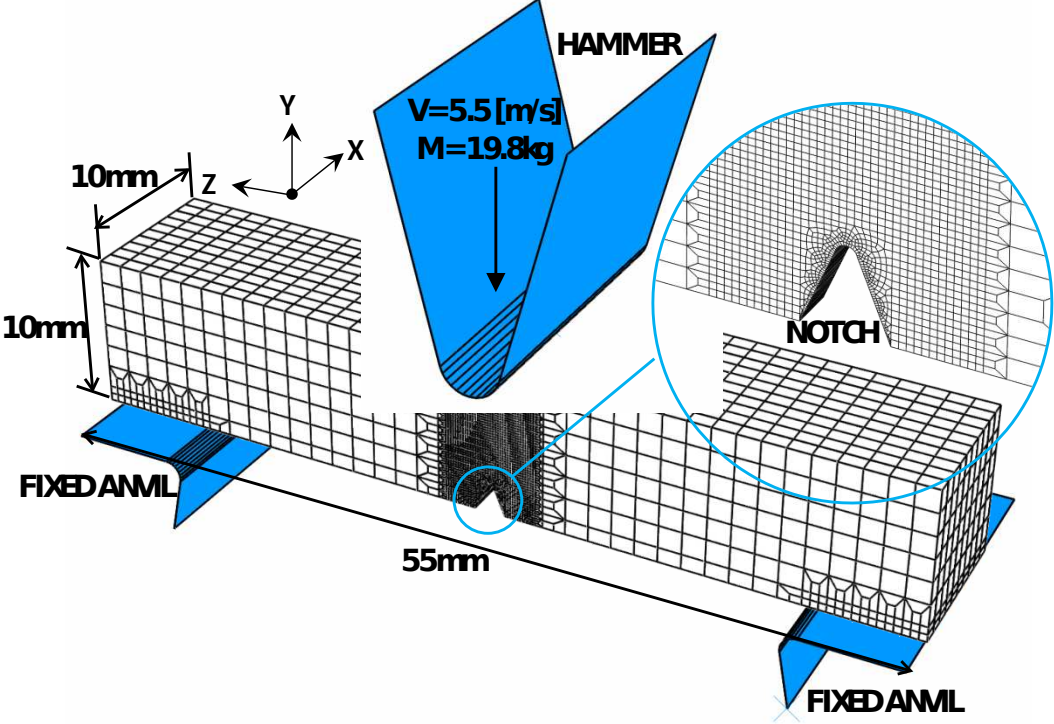
Figure 3 (double column image = 140mm width)
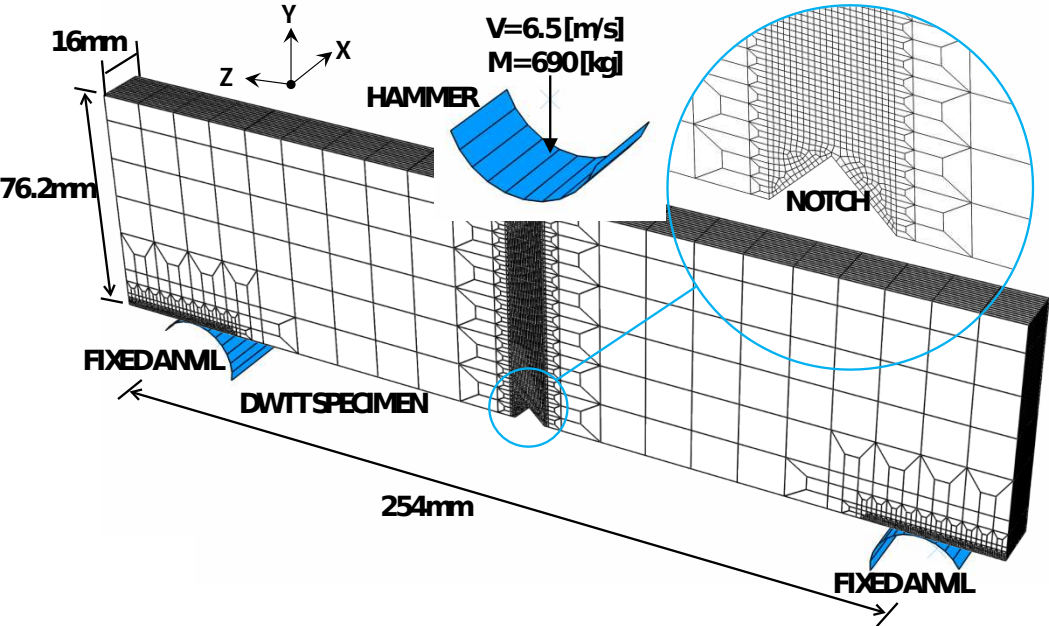
Figure 4 (double column image = 140mm width)
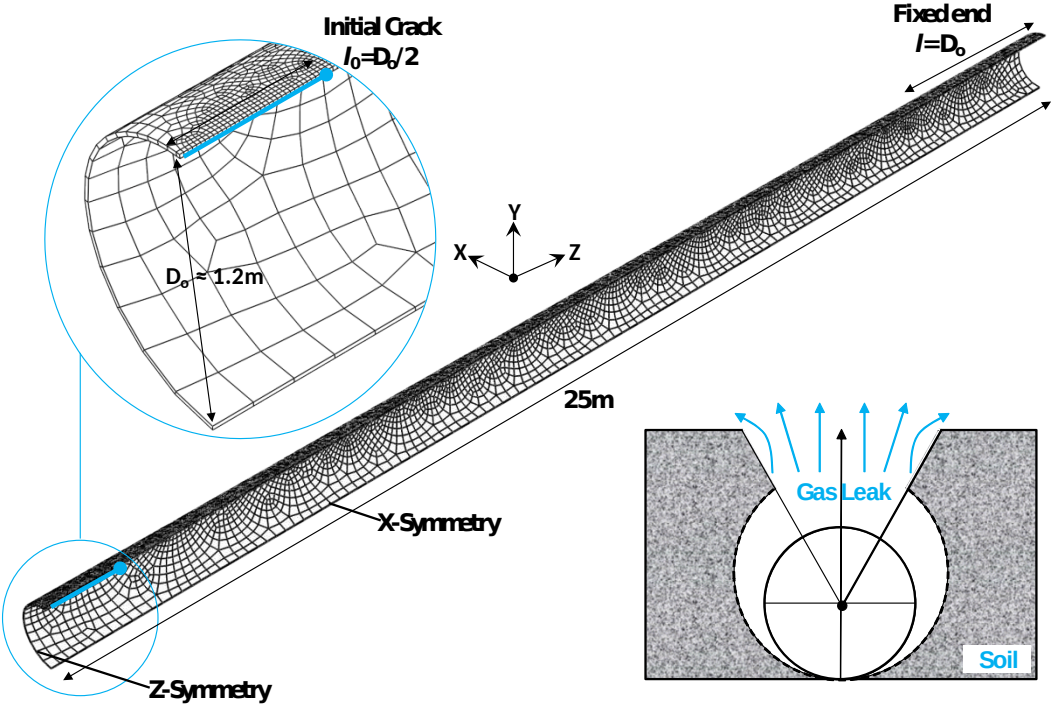
Figure 5 (single column image = 90mm width)
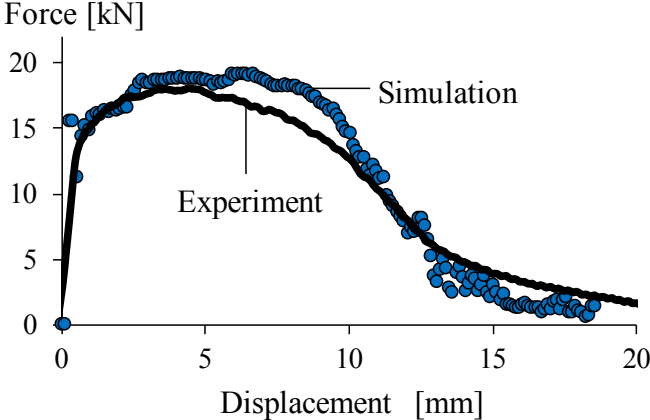
Figure 6 (single column image = 90mm width)
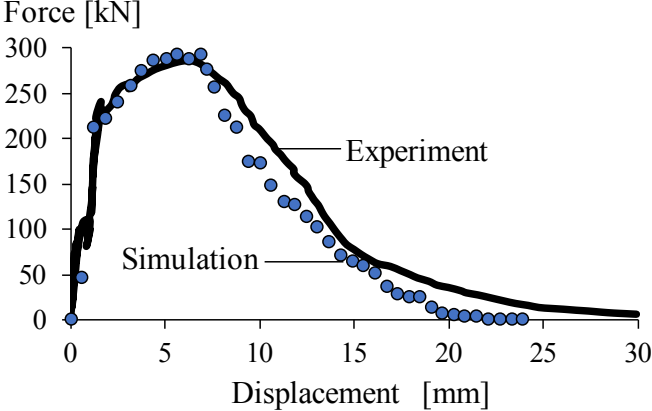
Figure 7 (double column image = 140mm width)

Max. Principal
Stress [MPa]

918
520
475
430
385
340
295
250
205
160
115
70
25
-20

[33]
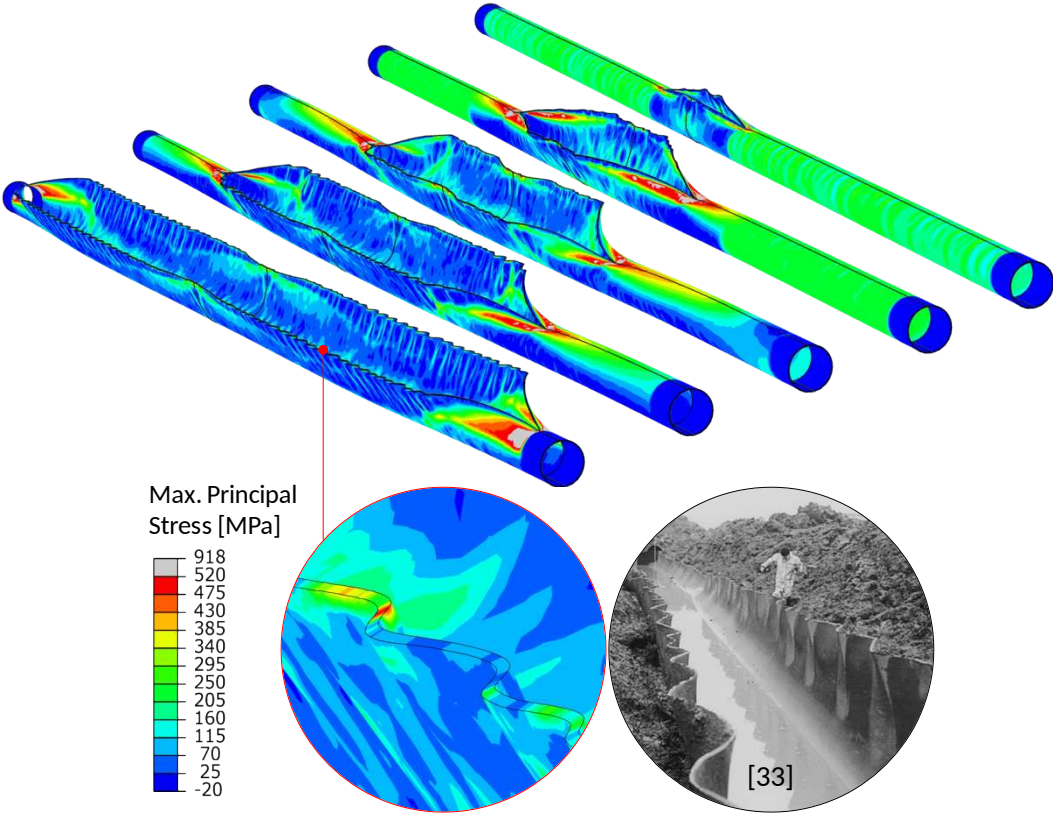
Figure 8 (double column image = 140mm width)
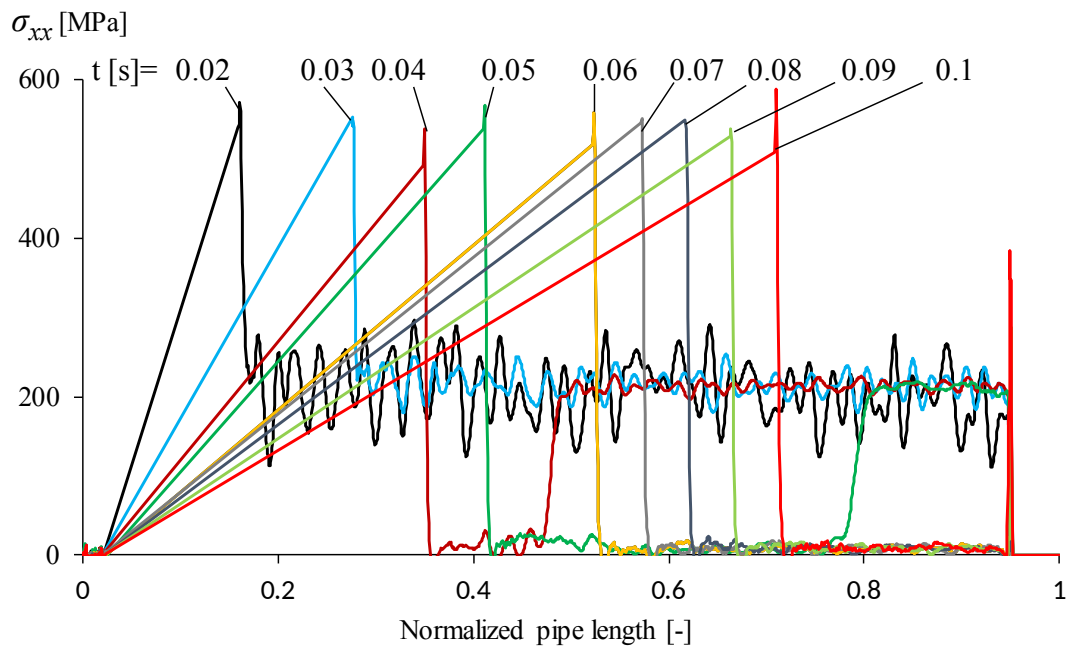

(a)
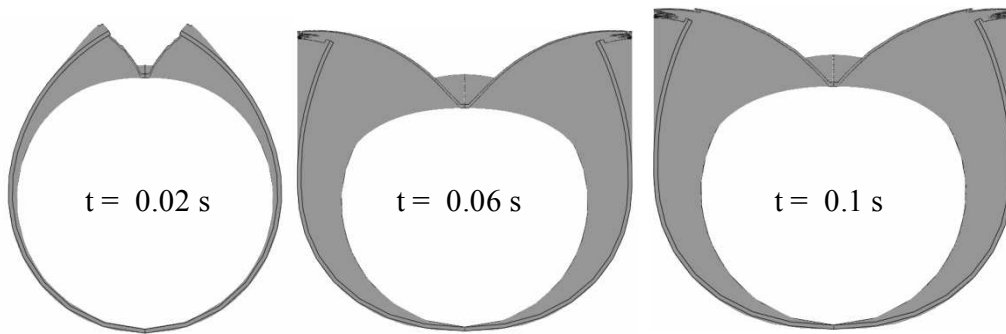
(b)

Figure 9 (single column image = 90mm width)
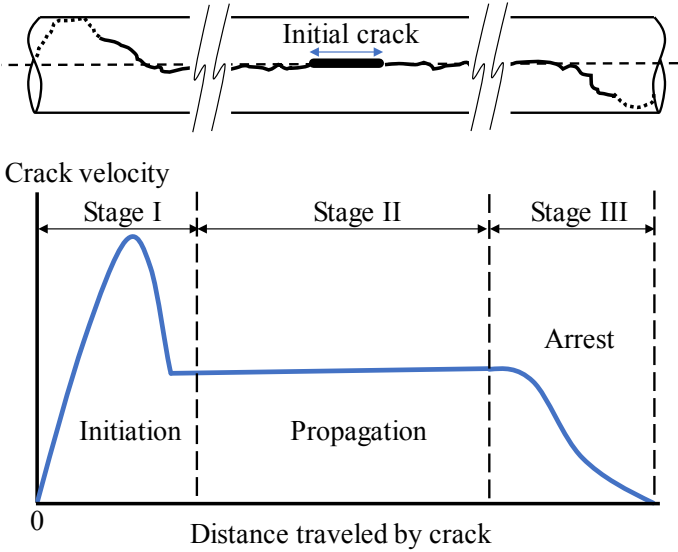
Figure 10 (double column image = 140mm width)